

© The Author(s) 2023. Rana, A., Liao, C.T., Iacocca, E. et al. Three-dimensional topological magnetic monopoles and their interactions in a ferromagnetic meta-lattice. Nat. Nanotechnol. (2023).

This version of the article has been accepted for publication, after peer review (when applicable) and is subject to Springer Nature's AM terms of use, but is not the Version of Record and does not reflect post-acceptance improvements, or any corrections. The Version of Record is available online at: <https://doi.org/10.1038/s41565-022-01311-0>

8 **Three-dimensional topological magnetic monopoles and their**
9 **interactions in a ferromagnetic meta-lattice**

10 Arjun Rana^{1,2,15}, Chen-Ting Liao^{2,3,15}, Ezio Iacocca^{4,5}, Ji Zou¹, Minh Pham^{2,6}, Xingyuan Lu^{1,7},
11 Emma-Elizabeth Cating Subramanian^{2,3}, Yuan Hung Lo^{1,2}, Sinéad A. Ryan^{2,3}, Charles S.
12 Bevis^{2,3}, Robert M. Karl Jr^{2,3}, Andrew J. Glaid⁸, Jeffrey Rable⁸, Pratibha Mahale^{8,9}, Joel Hirst¹⁰,
13 Thomas Ostler^{10,11}, William Liu^{1,2}, Colum M. O’Leary^{1,2}, Young-Sang Yu¹², Karen Bustillo¹³,
14 Hendrik Ohldag¹², David A. Shapiro¹², Sadegh Yazdi¹⁴, Thomas E. Mallouk^{8,9}, Stanley J.
15 Osher^{2,6}, Henry C. Kapteyn^{2,3}, Vincent H. Crespi⁸, John V. Badding⁸, Yaroslav Tserkovnyak¹,
16 Margaret M. Murnane^{2,3}, Jianwei Miao^{1,2*}

17 *¹Department of Physics & Astronomy and California NanoSystems Institute, University of*
18 *California, Los Angeles, CA 90095, USA. ²STROBE Science and Technology Center. ³JILA*
19 *and Department of Physics, University of Colorado and NIST, 440 UCB, Boulder, Colorado*
20 *80309, USA. ⁴Department of Mathematics, Physics, and Electrical Engineering, Northumbria*
21 *University, Newcastle upon Tyne, NE1 8ST, UK. ⁵Center for Magnetism and Magnetic*
22 *Materials, University of Colorado, Colorado Springs, CO 80918, USA. ⁶Department of*
23 *Mathematics, University of California, Los Angeles, CA 90095, USA. ⁷School of Physical*
24 *Science and Technology, Soochow University, Suzhou 215006, China. ⁸Departments of*
25 *Chemistry, Physics, Materials Science and Engineering and Materials Research Institute,*
26 *Penn State University, University Park, PA 16802, USA. ⁹Department of Chemistry, University*
27 *of Pennsylvania, Philadelphia PA 19104, USA. ¹⁰Materials and Engineering Research*
28 *Institute, Sheffield Hallam University, Howard Street, Sheffield S1 1WB, UK. ¹¹Department of*
29 *Physics and Mathematics, University of Hull, Cottingham Road, Hull, HU67RX, UK.*
30 *¹²Advanced Light Source, Lawrence Berkeley National Laboratory, Berkeley, CA 94720, USA.*
31 *¹³National Center for Electron Microscopy, Molecular Foundry, Lawrence Berkeley National*

32 *Laboratory, Berkeley, CA, 94720, USA.* ¹⁴*Renewable and Sustainable Energy Institute,*
33 *University of Colorado, Boulder, CO 80309, USA.*

34 ¹⁵*These authors contributed equally to this work. *email: miao@physics.ucla.edu*

35 **Topological magnetic monopoles (TMMs), also known as hedgehogs or Bloch points, are**
36 **three-dimensional (3D) nonlocal spin textures that are robust to thermal and quantum**
37 **fluctuations due to the topology protection¹⁻⁴. Although TMMs have been observed in**
38 **skyrmion lattices^{1,5}, spinor Bose–Einstein condensates^{6,7}, chiral magnets⁸, vortex rings^{2,9},**
39 **and vortex cores¹⁰, it has been difficult to directly measure the 3D magnetization vector**
40 **field of TMMs and probe their interactions at the nanoscale. Here, we report the creation**
41 **of 138 stable TMMs at the specific sites of a ferromagnetic meta-lattice at room**
42 **temperature. We further develop soft x-ray vector ptycho-tomography to determine the**
43 **magnetization vector and emergent magnetic field of the TMMs with a 3D spatial**
44 **resolution of 10 nm. This spatial resolution is comparable to the magnetic exchange length**
45 **of transition metals¹¹, enabling us to probe monopole-monopole interactions. We find that**
46 **the TMM and anti-TMM pairs are separated by 18.3 ± 1.6 nm, while the TMM and TMM,**
47 **anti-TMM and anti-TMM pairs are stabilized at comparatively longer distances of**
48 **36.1 ± 2.4 nm and 43.1 ± 2.0 nm, respectively. We also observe virtual TMMs created by**
49 **magnetic voids in the meta-lattice. This work demonstrates that ferromagnetic meta-**
50 **lattices could be used as a platform to create and investigate the interactions and**
51 **dynamics of TMMs. Furthermore, we expect that soft x-ray vector ptycho-tomography**
52 **can be broadly applied to quantitatively image 3D vector fields in magnetic and**
53 **anisotropic materials at the nanoscale.**

54 The 3D ferromagnetic meta-lattice was synthesized by self-assembly of a face-centred
55 cubic (fcc) template using silica nanospheres of 60 nm in diameter (Methods). The interstitial
56 spaces between the nanospheres of the template were infiltrated with nickel to create a meta-

57 lattice, comprising octahedral and tetrahedral sites interconnected by thin necks^{12,13}.
58 Superconducting quantum interference device (SQUID) measurements show that the saturation
59 magnetization of the meta-lattice is consistent with that of the nickel thin film (Extended Data
60 Fig. 1). The complex 3D curved surfaces of the silica nanospheres in the meta-lattice create a
61 magnetically frustrated configuration that could harbour topological spin textures. To
62 quantitatively characterize the topological spin textures, we developed soft x-ray vector
63 ptycho-tomography to directly determine the 3D magnetization vector field in the ferromagnetic
64 meta-lattice, which is in contrast to the 3D vector imaging methods using Maxwell's equations
65 as a constraint¹⁴⁻¹⁶. By measuring diffraction patterns with high differential magnetic contrast at
66 the L_3 -edge resonance of transition metals^{17,18}, we improved the spatial resolution close to the
67 magnetic exchange length of transition metals¹¹, which represents a significant advance of the
68 resolution over previous soft and hard x-ray vector tomography methods^{2,9,19-24}.

69 The experiment was conducted by focusing circularly polarized soft x-rays onto the
70 ferromagnetic meta-lattice at room temperature (Fig. 1). The magnetic contrast of the sample
71 was obtained by using x-ray magnetic circular dichroism (XMCD)^{14,18,25} and tuning the x-ray
72 energy to the L_3 -edge of nickel²⁶. To separate the magnetic contrast from the electron density,
73 two independent measurements were made with left- and right-circularly polarized soft x-rays.
74 In each measurement, three independent tilt series were acquired from the sample,
75 corresponding to three in-plane rotation angles (0° , 120° and 240°) around the z-axis (Fig. 1
76 and Extended Data Fig. 2). Each tilt series was collected by rotating the sample around the x-
77 axis with a tilt range from -62° to $+61^\circ$. At each tilt angle, a focused x-ray beam was scanned
78 over the sample with partial overlap between adjacent scan positions and a far-field diffraction
79 pattern was recorded by a charge-coupled device camera at each scan position (Methods). The
80 full data set consists of six tilt series with a total of 796,485 diffraction patterns.

81 The diffraction patterns were reconstructed using a regularized ptychographic iterative

82 engine²⁷, where corrupted diffraction patterns were removed and phase unwrapping was
83 implemented (Methods, Extended Data Fig. 3). Each pair of left- and right-circularly polarized
84 projections was aligned and converted to the optical density for normalization. The sum of each
85 pair of the oppositely polarized projections produced three independent tilt series
86 corresponding to three in-plane rotation angles. The scalar tomographic reconstruction was
87 performed from the three tilt series of 91 projections using a real space iterative algorithm
88 (Methods), which can optimize the reconstruction by iteratively refining the spatial and angular
89 alignment of the projections. Quantitative characterization of the reconstructed 3D electron
90 density and a scanning transmission electron microscopy image of the sample indicates that,
91 although there are some imperfections, the meta-lattice has an ordered fcc structure (Extended
92 Data Figs. 4 and 5a, b). To determine the magnetization vector field, we took the difference of
93 the left- and right-circularly polarized projections of the three tilt series (Extended Data Fig. 6).
94 The 3D vector reconstruction was performed from 91 difference projections by least-squares
95 optimization with gradient descent (Methods). Supplementary Video 1 shows the 3D electron
96 density and magnetization vector field in the ferromagnetic meta-lattice. To validate the 3D
97 vector reconstruction and quantify the spatial resolution, we divided all the projections into two
98 halves by choosing alternate projections and performed two independent 3D vector
99 reconstructions. By calculating the Fourier shell correlation from the two independent
100 reconstructions, we confirmed that a spatial resolution of 10 nm was achieved for the 3D vector
101 reconstruction of the magnetization field (Methods and Extended Data Fig. 7).

102 Next, we analyzed the experimental 3D magnetization vector field focusing on the
103 topological aspects. We characterized TMMs in the ferromagnetic meta-lattice that are robust
104 to thermal or quantum fluctuations due to the topological protection. In 3D magnetic systems,
105 a TMM within a volume Ω follows the volume-surface relationship⁴ (i.e., the divergence
106 theorem),

107
$$Q = \int_{\Omega} \rho \, dx dy dz = \int_{\partial\Omega} \mathbf{B}_e \cdot d\mathbf{S}, \quad (1)$$

108 where Q is the topological charge with the charge density $\rho = \frac{3}{4\pi} \partial_x \mathbf{n} \cdot (\partial_y \mathbf{n} \times \partial_z \mathbf{n})$, $\partial\Omega$ is the
 109 bounding surface, \mathbf{n} is the normalized magnetization vector field, $B_e^i = \frac{1}{8\pi} \epsilon^{ijk} \mathbf{n} \cdot (\partial_j \mathbf{n} \times$
 110 $\partial_k \mathbf{n})$ is the emergent magnetic field satisfying $\nabla \cdot \mathbf{B}_e = \rho$, and ϵ^{ijk} is the Levi-Civita symbol.
 111 \mathbf{B}_e acts on (quasi)particles such as electrons and magnons moving through the magnetic texture
 112 as long as they carry a spin³, which has been previously investigated in theory and
 113 experiment^{4,9,20,28}. The right-hand side of equation (1) is commonly used to evaluate the
 114 skyrmion number in a 2D plane^{29,30}, but can be generalized to any 3D embedded surface. When
 115 the magnetization vectors on the surface of a sphere enclosing a volume Ω covers the
 116 orientational parameter space exactly once, we have the topological charge $Q = \pm 1$, where +1
 117 and -1 represent a TMM and an anti-TMM, respectively. It is important to note that skyrmions
 118 and TMMs are fundamentally different spin textures. Skyrmions are local textures and can be
 119 annihilated by shrinking their cores down to the lattice constant without affecting the spin states
 120 far away^{29,30}. In contrast, TMMs are nonlocal spin textures and robust to local fluctuations¹⁻⁴.
 121 They are topologically protected, that is, the volume-surface relationship of equation (1) holds
 122 even when the system is not well-ordered. TMMs can only be removed by the outflow of a
 123 topological current through the boundary or annihilated in oppositely charged pairs.

124 Although we used the normalized magnetization vector field (\mathbf{n}) in this study, equation
 125 (1) holds even when \mathbf{n} varies in its magnitude⁴. To apply equation (1) to the ferromagnetic meta-
 126 lattice, we computed the local maxima and minima of the topological charge density within the
 127 volume of the sample. At each local extremum, we defined an enclosed surface and calculated
 128 the topological charge (Methods). Figure 2a and Supplementary Video 2 show the 3D spatial
 129 distribution of 68 TMMs (red dots) and 70 anti-TMMs (blue dots) in the meta-lattice. We
 130 observed that 90 TMMs and anti-TMMs are located in the octahedral sites, and 48 in the
 131 tetrahedral sites and the thin neck regions, which is likely due to a larger total volume of the

132 octahedral sites than the tetrahedral sites. Figure 2b and d show a representative TMM and anti-
133 TMM located in an octahedral and tetrahedral site, respectively. Since their 3D spin textures
134 exhibit a circulating configuration (Fig. 2c and e), the sign of the charge is not apparent from
135 the 3D spin textures, but can be unambiguously observed from the emergent magnetic field
136 (Extended Data Fig. 8a and b).

137 The existence of a large number of TMMs in the ferromagnetic meta-lattice allowed us
138 to probe their interactions. According to monopole confinement theory⁴, the potential energy of
139 a monopole pair with a positive and negative charge grows linearly with their separation when
140 the exchange energy dominates, with all the emergent magnetic field lines emanating from the
141 positive charge and ending at the negative charge. A non-negligible pair separation indicates
142 the existence of other interactions competing with the exchange energy. Figure 3a shows a
143 representative TMM and anti-TMM pair, where the emergent magnetic field lines were
144 computed from the magnetization vector field using equation (1). We observed that only part
145 of the magnetic flux emanating from the TMM terminates at the anti-TMM, indicating that the
146 emergent magnetic field lines are not completely confined. In comparison, the emergent
147 magnetic field lines in similarly charged pairs exhibit repulsive interactions (Fig. 3b and c).
148 The distance of the TMM and anti-TMM pairs was fit to be 18.3 ± 1.6 nm using a generalized
149 extreme value distribution that accounts for the asymmetry in the measured distance
150 distribution (Fig. 3d), while the TMM and TMM, anti-TMM and anti-TMM pairs were stabilized
151 at longer distances of 36.1 ± 2.4 nm and 43.1 ± 2.0 nm (Fig. 3e and f), respectively. The
152 statistically significant shorter distance of the TMM and anti-TMM pairs than the two other
153 pair distances is consistent with theory⁴, indicating that the system is under near equilibrium
154 conditions.

155 To investigate the effects of the experimental errors and statistical fluctuations on the
156 analysis of TMMs, we added random angular fluctuations to the experimentally measured

157 magnetization vectors with a standard deviation of 2° , 15° and 20° . We then calculated the
158 topological charges using equation (1). Extended Data Fig. 9a-b show the histograms of the
159 topological charge as a function of the random angular fluctuation, showing two sharp peaks
160 with $Q = \pm 1$ due to the quantization of the topological charge. After applying an angular
161 fluctuation of 2° to the magnetization vectors, we identified 68 TMMs and 69 anti-TMMs.
162 With the increase of the angular fluctuation to 15° and 20° , the number of TMMs became 72
163 and 65, while the number of anti-TMMs was changed to 65 and 66, respectively. We also
164 statistically calculated the nearest-neighbour distances of the TMM and anti-TMM, TMM and
165 TMM, anti-TMM and anti-TMM pairs for the angular fluctuation of 2° , 15° and 20° (Extended
166 Data Fig. 9d-l), which are consistent with those without the introduction of the angular
167 fluctuation (Fig. 3d-f). This analysis confirmed that our experimental observations are real and
168 cannot be due to statistical fluctuations or noise. To examine if the imperfections in the sample
169 affect the interactions of the TMMs, we chose a more ordered region in the meta-lattice and
170 plotted the histogram of the nearest-neighbour distances between oppositely and similarly
171 charged TMMs in the region (Extended Data Fig. 5), which agree with that obtained from a
172 larger region including some imperfections (Fig. 3d-f). The consistency of the two histograms
173 corroborated that the structural imperfections in the meta-lattice do not play a significant role
174 in influencing the interactions of the TMMs.

175 Due to the high surface to volume ratio of the meta-lattice, some TMMs and anti-TMMs
176 could escape through the 3D internal surfaces of the magnetic voids created by the silica
177 nanospheres. Because the topological charge is conserved, an escaped TMM or anti-TMM
178 would produce a $Q = +1$ or -1 charge on an internal surface, respectively. To experimentally
179 investigate this phenomenon, we performed a non-convex triangulation of the 3D internal
180 surfaces in the meta-lattice. The resulting facets were grouped into individual void surfaces by a
181 community-clustering technique used in network analysis³¹. As the majority of the magnetic voids

182 are not fully closed due to the finite thickness of the sample, we defined any void surface with
183 $Q \geq 0.9$ as a virtual TMM and $Q \leq -0.9$ as a virtual anti-TMM. Using equation (1), we found
184 8 virtual TMMs and 11 virtual anti-TMMs in the ferromagnetic meta-lattice (Fig. 2a and
185 Supplementary Video 2). Two representative virtual TMMs with $Q = 1.01$ and -1 are shown
186 in Fig. 4a and b, respectively. The 3D magnetization vector field on the two magnetic voids
187 was mapped onto a 2D plane to produce two stereographic projections, exhibiting skyrmion
188 and anti-skyrmion configurations (Fig. 4c and d). For the virtual TMM, most spins point down
189 in the centre and up at the boundary, while for the virtual anti-TMM, most spins point up in the
190 centre and down at the boundary. The emergent magnetic field of the virtual TMM and anti-
191 TMM shows features as if a real TMM and anti-TMM reside at the geometric centres of the
192 magnetic voids (Extended Data Fig. 8c and d), which is a clear manifestation of the volume-
193 surface correspondence.

194 Compared to materials systems that usually support topological defects, such as non-
195 centrosymmetric lattices and magnetic / heavy-metal multilayers^{1,29,30}, the ferromagnetic meta-
196 lattice studied does not possess strong anisotropy or the Dzyaloshinskii-Moriya interaction
197 (DMI). However, surface curvature can stabilize magnetic solitons through the effective
198 DMI^{32,33}. The complex 3D curved surface of the magnetic voids induces strong frustration in
199 the ferromagnetic meta-lattice, which can stabilize TMMs at the octahedral and tetrahedral sites
200 of the meta-lattice. Similar stable TMM and anti-TMM pairs with a nanometre distance have
201 been reported in a frustrated ferrimagnet based on first-principle simulations³⁴, although the
202 frustration has a different origin from our system. Using our experimental data as direct input
203 to atomistic simulations, we numerically demonstrated that TMMs can be stabilized by the
204 boundary conditions (Methods). We extracted four $15 \times 15 \times 15 \text{ nm}^3$ volumes from the
205 ferromagnetic meta-lattice, containing two TMMs and two anti-TMMs. The atomistic spins on
206 the outer boundary of each volume were fixed, while all the other spins were allowed to relax

207 to an equilibrium configuration. After 50 ps, a stable TMM or anti-TMM formed in each
208 volume with a topological charge matching the experimental value (Extended Data Fig. 10a-
209 d). We also observed that as long as the atomistic spins were fixed on four of the six surfaces
210 of each volume, the TMM or anti-TMM remained stable inside the volume (Extended Data
211 Fig. 10e-h). These results further confirmed that surface constraints can stabilize TMMs and
212 anti-TMMs, although the detailed mechanism requires further investigation.

213 In conclusion, we have created and directly observed TMMs and their interactions in a
214 ferromagnetic meta-lattice with a 3D spatial resolution of 10 nm. This work could open the
215 door to use magnetically frustrated meta-lattices as a new platform to study the interactions,
216 dynamics, and confinement-deconfinement transition of TMMs⁴. Furthermore, as a powerful
217 scanning coherent diffractive imaging method³⁵⁻³⁸, the 3D spatial resolution of soft x-ray vector
218 ptycho-tomography can be improved by increasing the incident coherent flux or the data
219 acquisition time. With the rapid development of advanced synchrotron radiation, x-ray free
220 electron lasers and high harmonic generation sources worldwide³⁶, we expect that soft-x-ray
221 vector ptycho-tomography can find broad applications in the topological spin texture,
222 nanomagnetism and x-ray imaging fields.

223

224 **Acknowledgements** We thank Rafal Dunin-Borkowski and Jong E. Han for stimulating
225 discussions and Yakun Yuan and Yao Yang for help with data analysis. This work was
226 primarily supported by STROBE: a National Science Foundation Science and Technology
227 Center under award DMR1548924. J.M. and A. R. acknowledge support by the US Department
228 of Energy, Office of Science, Basic Energy Sciences, Division of Materials Sciences and
229 Engineering under award number DE-SC0010378 for the contribution to the development of
230 vector ptycho-tomography. J.M. thanks partial support by the Army Research Office MURI
231 program under grant no. W911NF-18-1-0431. M.M.M. and H.C.K. acknowledge partial

232 support by the US Department of Energy, Office of Science, Basic Energy Sciences X-
233 Ray Scattering Program Award DE-SC0002002 and DARPA TEE Award No. D18AC00017
234 for the data acquisition and analysis. Y.T. and J.Z. were supported by the U.S. Department of
235 Energy, Office of Basic Energy Sciences under Grant No. DE-SC0012190. Soft x-ray ptycho-
236 tomography experiments were performed at COSMIC used resources of the Advanced Light
237 Source, which is a DOE Office of Science User Facility under contract no. DE-AC02-
238 05CH11231.

239 **Author contributions** J.M. directed the project; M.M.M. suggested the sample; A.J.G, J.V.B,
240 P.M., T.E.M., C.-T.L. and S.Y. synthesized and fabricated the sample; A.R., C.-T.L., Y.H.L.,
241 E.E.C.S., S.R., X.L., C.S.B., R.M.K., A.J.G., J.R., H.O., Y.S.Y., D.A.S, H.C.K., M.M.M. and
242 J.M. planed and/or performed the experiments; M.P., A.R., S.J.O. and J.M. developed the
243 scalar and vector tomography algorithms; A.R. and J.M. reconstructed the 3D magnetization
244 vector field; A.R., E.I. J.Z., X.L. and J.M. analysed the data with input from M.M.M., Y.T.,
245 C.-T.L., W.L. and V.H.C.; J.H., T.O., E.I. and J.M. discussed and/or conducted the atomistic
246 simulations; A.R., J.M., E.I. and J.Z. wrote the manuscript with input from M.M.M., Y.T., C.-
247 T.L., S.Y., E.E.C.S. and T.E.M.

248 **Competing interests** The authors declare no competing interests.

249

250 **Figures legends**

251 **Fig. 1. Experimental schematic of soft x-ray vector ptycho-tomography.** **a**, Left- and right-
252 circularly polarized x-rays (pink) were focused onto a ferromagnetic meta-lattice sample
253 (centre), on which the green circles indicate the partially overlapped scan positions. The sample
254 was tilted around the x- and z-axis and diffraction patterns were collected by a detector. **b**, 3D
255 electron density (green) and magnetization vector field (arrows) in the meta-lattice
256 reconstructed from the diffraction patterns. A magnified magnetization vector field is shown

257 in Supplementary Video 1.

258 **Fig. 2. Quantitative 3D characterization of TMMs in the ferromagnetic meta-lattice. a,**
 259 3D spatial distribution of 68 TMMs (red dots) and 70 anti-TMMs (blue dots) in the meta-lattice,
 260 where the surfaces of the magnetic voids in red and blue blobs represent virtual TMMs and
 261 anti-TMMs, respectively. The solid and dashed squares mark the region of interest shown in
 262 (b) and (d), respectively. b, c, The location and 3D spin textures of a TMM within a tetrahedral
 263 site of the fcc meta-lattice. d, e, The location and 3D spin textures of an anti-TMM within an
 264 octahedral site. Scale bars, 60 nm (a); 25 nm (b); and 10 nm (c). Note that the voxel size of the
 265 magnetization vector field is $5 \times 5 \times 5 \text{ nm}^3$, which is set by the experiment, but the 3D spatial
 266 resolution was characterized to be 10 nm (Methods).

267 **Fig. 3. Interactions of the TMMs in the ferromagnetic meta-lattice. a-c,** A TMM and anti-
 268 TMM pair (a), a TMM and TMM pair, and (b) and a TMM and anti-TMM pair (c), where the
 269 continuous and smooth white lines represent the magnetic field lines the magnetic field lines
 270 calculated from the emergent magnetic field of each voxel. d-f, Histograms of the nearest-
 271 neighbour distances for the TMM and anti-TMM pairs (d), the TMM and TMM pairs (e), and
 272 the anti-TMM and anti-TMM pairs (f). The three histograms were fit to a generalized extreme
 273 value distribution, producing three curves in (d-f), where μ represents the centre of each fit and
 274 the standard error was determined from the fit's 95% confidence interval. Scale bar, 5 nm.

275 **Fig. 4. Representative virtual TMMs in the ferromagnetic meta-lattice. a, b,** Two virtual
 276 TMMs with $Q = 1.01$ and -1 , respectively, where the arrows indicate the 3D magnetization
 277 vector field. c, d, Stereographic projections of the virtual TMMs shown in (a) and (b)
 278 exhibiting skyrmion (c) and anti-skyrmion configurations (d). The colours of the arrows
 279 represents the z-component of the spin with pointing up (+z) in red and down (-z) in blue. Scale
 280 bar, 15 nm.

281

282 **References**

- 283 1. Milde, P. et al. Unwinding of a skyrmion lattice by magnetic monopoles. *Science* **340**, 1076–
284 1080 (2013).
- 285 2. Donnelly, C. et al. Three-dimensional magnetization structures revealed with X-ray vector
286 nanotomography. *Nature* **547**, 328–331 (2017).
- 287 3. Tataru, G. & Nakabayashi, N. Emergent spin electromagnetism induced by magnetization
288 textures in the presence of spin-orbit interaction. *J. Appl. Phys.* **115**, 172609 (2014).
- 289 4. Zou, J., Zhang, S. & Tserkovnyak, Y. Topological transport of deconfined hedgehogs in
290 magnets. *Phys. Rev. Lett.* **125**, 267201 (2020).
- 291 5. Yu, X. et al. Real-Space Observation of Topological Defects in Extended Skyrmion-Strings.
292 *Nano Lett.* **20**, 7313–7320 (2020).
- 293 6. Pietilä, V & Möttönen, M. Creation of Dirac monopoles in spinor Bose-Einstein condensates.
294 *Phys. Rev. Lett.* **103**, 030401 (2009).
- 295 7. Ray, M. W., Ruokokoski, E., Kandel, S., Möttönen, M. & Hall, D. S. Observation of Dirac
296 monopoles in a synthetic magnetic field. *Nature* **505**, 657–660 (2014).
- 297 8. Kanazawa, N. et al. Critical phenomena of emergent magnetic monopoles in a chiral magnet.
298 *Nat. Commun.* **7**, 11622 (2016).
- 299 9. Donnelly, C. et al. Experimental observation of vortex rings in a bulk magnet. *Nat. Phys.* **17**,
300 316–321 (2021).
- 301 10. Im, M.-Y. et al. Dynamics of the Bloch point in an asymmetric permalloy disk. *Nat. Commun.*
302 **10**, 593 (2019).
- 303 11. Abo, G. S. et al. Definition of Magnetic Exchange Length. *IEEE Trans. Magn.* **49**, 4937-4939
304 (2013).
- 305 12. Han, J. E. & Crespi, V. H. Abrupt Topological Transitions in the Hysteresis Curves of
306 Ferromagnetic Metalattices. *Phys. Rev. Lett.* **89**, 197203 (2002).
- 307 13. Liu, Y. et al. Confined chemical fluid deposition of ferromagnetic metalattices. *Nano Lett.* **18**,
308 546–552 (2018).
- 309 14. Phatak, C., Petford-Long, A. K. & De Graef, M. Three-dimensional study of the vector potential

- 310 of magnetic structures. *Phys. Rev. Lett.* **104**, 253901 (2010).
- 311 15. Phatak, C. , Heinonen, O., De Graef, M. & Petford-Long, A. K. Nanoscale skyrmions in a
312 nonchiral metallic multiferroic: Ni₂MnGa. *Nano Lett.* **16**, 4141–4148 (2016).
- 313 16. Davis, T. J., Janoschka, D., Dreher, P. & Frank, B. Ultrafast vector imaging of plasmonic
314 skyrmion dynamics with deep subwavelength resolution. *Science* **368**, eaba6415 (2020).
- 315 17. Streubel, R. et al. Retrieving spin textures on curved magnetic thin films with full-field soft X-
316 ray microscopies. *Nat. Commun.* **6**, 1–11 (2015).
- 317 18. Stöhr, J. & Siegmann, H. C. *Magnetism: From Fundamentals to Nanoscale Dynamics* 1st edn
318 (Springer, 2006).
- 319 19. Donnelly, C. et al. Time-resolved imaging of three-dimensional nanoscale magnetization
320 dynamics. *Nat. Nanotechnol.* **15**, 356–360 (2020).
- 321 20. Hierro-Rodriguez, A. et al. Revealing 3D magnetization of thin films with soft X-ray
322 tomography: magnetic singularities and topological charges. *Nat. Commun.* **11**, 6382 (2020).
- 323 21. Witte, K. et al. From 2D STXM to 3D Imaging: Soft X-ray Laminography of Thin Specimens.
324 *Nano Lett.* **20**, 1305–1314 (2020).
- 325 22. Josten, E. et al. Curvature-mediated spin textures in magnetic multi-layered nanotubes. Preprint
326 at <https://arxiv.org/abs/2103.13310> (2021).
- 327 23. Donnelly, C. et al. Complex free-space magnetic field textures induced by three-dimensional
328 magnetic nanostructures. *Nat. Nanotechnol.* **17**, 136–142 (2022).
- 329 24. Hermosa-Muñoz, J. et al. 3D magnetic configuration of ferrimagnetic multilayers with
330 competing interactions visualized by soft X-ray vector tomography. *Commun. Phys.* **5**, 26
331 (2022).
- 332 25. Tripathi, A. et al. Dichroic coherent diffractive imaging. *Proc. Natl. Acad. Sci. USA* **108**,
333 13393–13398 (2011).
- 334 26. Chen, C. T., Sette, F., Ma, Y. & Modesti, S. Soft-x-ray magnetic circular dichroism at the L_{2,3}
335 edges of nickel. *Phys. Rev. B* **42**, 7262–7265 (1990).
- 336 27. Maiden, A., Johnson, D. & Li, P. Further improvements to the ptychographical iterative engine.
337 *Optica* **4**, 736–745 (2017).

- 338 28. Volovik, G. E. Linear momentum in ferromagnets. *J. Phys. C Solid State Phys.* **20**, L83–L87
339 (1987).
- 340 29. Nagaosa, N. & Tokura, Y. Topological properties and dynamics of magnetic skyrmions. *Nat.*
341 *Nanotechnol.* **8**, 899–911 (2013).
- 342 30. Fert, A., Reyren, N. & Cros, V. Magnetic skyrmions: advances in physics and potential
343 applications. *Nat. Rev. Mater.* **2**, 1–15 (2017).
- 344 31. Jain, A. K., Murty, M. N. & Flynn, P. J. Data clustering: a review. *ACM Comput. Surv.* **31**,
345 264–323 (1999).
- 346 32. Streubel, R. et al. Magnetism in curved geometries. *J. Phys. D. Appl. Phys.* **49**, 363001 (2016).
- 347 33. Vitelli, V. & Turner, A. M. Anomalous coupling between topological defects and curvature.
348 *Phys. Rev. Lett.* **93**, 215301 (2004).
- 349 34. Bayaraa, T., Xu, C. & Bellaiche, L. Magnetization Compensation Temperature and Frustration-
350 Induced Topological Defects in Ferrimagnetic Antiperovskite Mn_4N . *Phys. Rev. Lett.* **127**,
351 217204 (2021).
- 352 35. Miao, J., Charalambous, P., Kirz, J. & Sayre, D. Extending the methodology of X-ray
353 crystallography to allow imaging of micrometre-sized non-crystalline specimens. *Nature* **400**,
354 342 (1999).
- 355 36. Miao, J., Ishikawa, T., Robinson, I. K. & Murnane, M. Beyond crystallography: Diffractive
356 imaging using coherent x-ray light sources. *Science* **348**, 530-535 (2015).
- 357 37. Rodenburg, J. M. et al. Hard-x-ray lensless imaging of extended objects. *Phys. Rev. Lett.* **98**,
358 34801 (2007).
- 359 38. Thibault, P. et al. High-Resolution Scanning X-ray Diffraction Microscopy. *Science* **321**, 379–
360 382 (2008).

361 **METHODS**

362 **Sample synthesis and preparation.** The 3D ferromagnetic meta-lattice was synthesized by infiltrating
363 interconnected voids of a silica nanoparticle template using confined chemical fluid deposition¹³. Monodisperse
364 silica nanoparticles of 60 nm in diameter (standard deviation < 5%) were synthesized using a liquid-phase
365 method³⁹. The evaporation-assisted vertical deposition technique was used to assemble these particles onto silicon
366 substrate⁴⁰. Briefly, 3 cm x 1 cm silicon wafers were placed at a ~30° angle in open plastic vials containing 10x

367 dilute solution of the as-synthesized particles. The vials were left undisturbed for two weeks in an oven maintained
368 at 40° C at 80% relative humidity. The resulting films that were used as the template for nickel infiltration
369 contained silica particles arranged in a fcc structure and had thicknesses ranging from 240 nm – 850 nm depending
370 on the vertical position of the silicon substrate⁴¹.

371 The infiltration of nickel within the template voids was performed using confined chemical fluid
372 deposition¹³. The template was spatially confined using a 250 μm thick U-shaped titanium spacer and placed
373 within a custom-built reactor made of parts from High Pressure Equipment Company, McMaster, and Swagelok.
374 Bis(cyclopentadienyl) nickel (II) was loaded into the reactor in a Vacuum Atmospheres argon glovebox. The
375 reactor was pressurized with Praxair 4.0 Industrial Grade carbon dioxide using a custom-made manual pump and
376 heated to 70°C for 8 hours at a pressure of around 13.8 MPa to dissolve the precursor powder into the supercritical
377 carbon dioxide. A separate gas reservoir was loaded with Praxair 5.0 ultra-high purity hydrogen using a Newport
378 Scientific Two Stage 207 MPa Diaphragm Pump and was connected to the reactor. The hydrogen was added to
379 the reactor to a final reactor pressure of 42.7 MPa and the deposition proceeded at 100°C for 10 hours. The
380 interstitial voids between the nanospheres of the template were then infiltrated with nickel, forming a meta-lattice.
381 An overfilled nickel film over the meta-lattice and template resulting from the deposition process was milled using
382 a Leica EM TIC 3x Argon ion beam milling system at 3° and 3 kV. The meta-lattice consists of octahedral and
383 tetrahedral sites with the size around 25 nm and 14 nm, respectively, which are interconnected by thin necks with
384 a varying thickness as small as ~5 nm. The distance between two nearest octahedral sites is ~60 nm, between two
385 nearest tetrahedral sites ~43 nm, and between two nearest octahedral and tetrahedral sites ~37 nm. The geometry
386 of the meta-lattice with a detailed schematic can be found elsewhere¹².

387 To prepare the meta-lattice sample the vector ptycho-tomography experiment, we lifted out a portion of
388 the sample from the bulk meta-lattice on a silicon substrate and thinned the sample using a focused ion beam (FIB,
389 FEI Nova 600 NanoLab DualBeam), which was equipped with a field emission scanning electron microscope and
390 a scanning gallium ion beam. The FIB prepared sample was mounted on a 3-mm TEM grid (Omniprobe, 3 posts
391 copper lift-out grid), where the central post was also trimmed by FIB milling to increase the tilt range. The sample
392 mounted on the TEM grid was examined by the scanning electron microscope and an optical microscope, and
393 then manually glued on a 3-mm copper ring using a silver paste (Extended Data Fig. 2a-f). The sample fabricated
394 by this process can be manually rotated in-plane for the vector ptycho-tomography experiment. To examine the
395 surface oxidation of the sample, we conducted an x-ray absorption spectroscopy experiment of the nickel meta-
396 lattice. By carefully analysing the x-ray absorption spectrum in comparison with that of a pure nickel film and a
397 NiO film⁴² (Extended Data Fig. 2g), we concluded that the surface oxide layer of the sample is very thin, which
398 is consistent with the previous experimental measurements⁴³.

399 **The soft x-ray vector ptycho-tomography experiment.** The experiment was conducted at the COSMIC beam
400 line at the Advanced Light Source, Lawrence Berkeley National Lab⁴⁴. Figure 1 shows the experimental schematic
401 of soft x-ray vector ptycho-tomography. An elliptical polarization undulator was used to generate circularly
402 polarized x-rays of left- and right-helicity and achieve differential contrast enhancement of the magnetic signal.
403 The incident photon energy was tuned to 856 eV, slightly above the nickel L₃ edge, to obtain the magnetic contrast
404 based on XMCD^{17,18,25,26,45}. The polarized beam was focused onto the sample by a Fresnel zone plate with an outer
405 width of 45 nm. A total of six tilt series with a tilt range from -62° to +61° were acquired from the sample with
406 left- and right-circularly polarized x-rays at three in-plane rotation angles (0°, 120° and 240°). At each tilt angle,

407 the focused beam was raster-scanned across the sample in 40 nm steps. Diffraction patterns were collected using
 408 both left- and right-circularly polarized x-rays. A charge-coupled device camera was used to record the diffraction
 409 patterns at each scan position. Initial reconstructions were performed on-site in real time using a GPU-based
 410 ptychography reconstruction algorithm⁴⁶.

411 **Data processing and ptychographic reconstructions.** A very small number of corrupted diffraction patterns,
 412 most commonly caused by detector readout malfunction or unstable beam flux, resulted in a global degradation
 413 of the reconstruction through the coupling of the probe and object. We used the following procedure to
 414 automatically detect and remove the corrupted diffraction patterns to achieve the high-quality reconstruction. The
 415 high-angle diffraction intensity at each scan position was integrated to produce a low-resolution map at every
 416 ptychography scan. Local maxima in the magnitude of the gradient of this map were used to identify and remove
 417 bad frames (Extended Data Fig. 3a and b). The image reconstructions were performed by using the regularized
 418 ptychographic iterative engine²⁶ coupled with phase unwrapping for high tilt angles⁴⁷ (Extended Data Fig. 3c and
 419 d). Specifically, for the first 10 iterations of the ptychographic reconstruction, no phase unwrapping was enforced.
 420 After that, phase unwrapping was applied to the object in every 3rd iteration. The final reconstruction was obtained
 421 with a total of 500 iterations.

422 From the reconstructed complex-valued exit wave, the absorption component was used as the magnetic
 423 contrast^{18,25} and the two oppositely-polarized projections at each tilt angle were aligned using a feature-based
 424 image registration package in MATLAB. The projections were converted to the optical density⁴⁸ by taking the
 425 logarithm of the ratio of the signal to the mean of the background region (i.e., outside the sample), which was
 426 used to normalize any small temporal and polarization-based fluctuations of the beam intensity. In each projection,
 427 background subtraction was performed by numerically evaluating Laplace's equation,

$$428 \quad \nabla^2 \varphi = 0 \quad , \quad (2)$$

429 where $\nabla^2 = \frac{\partial^2}{\partial x^2} + \frac{\partial^2}{\partial y^2}$ is the 2D Laplace operator and φ represents the background of the projection. To determine
 430 φ , we solved equation (2) by using the region exterior to the sample as the boundary condition. The value at the
 431 boundary corresponds to the optical density in vacuum. Mathematically, the calculation of φ is equivalent to the
 432 determination of the geometry of a soap film from an enclosed boundary. We implemented this procedure by
 433 using a MATLAB function called 'regionfill'. We found that this method outperforms simple constant background
 434 subtraction by taking into account the local variation of the background⁴⁹.

435 **The scalar tomography reconstruction.** The relationship between charge and magnetic scattering^{18,25,50},

$$f = f^c \pm i f^m \hat{z} \cdot \mathbf{m} \quad , \quad (3)$$

436 was used to generate a set of scalar and vector projections corresponding to the charge and magnetic scattering,
 437 where f^c and f^m are the charge and magnetic scattering factor, respectively, \hat{z} is the x-ray propagation direction,
 438 and \mathbf{m} is the magnetization vector. The sum of each pair of the oppositely-polarized projections produced three
 439 independent tilt series corresponding to three in-plane rotation angles. The scalar projections of each tilt series were
 440 first roughly aligned with cross-correlation, then more accurately aligned using the centre-of-mass and common
 441 line method^{51,52}. The aligned tilt series was reconstructed by a real space iterative reconstruction (RESIRE)
 442 algorithm⁴⁹, which was able to iteratively perform angular and spatial refinement to adjust any remaining small
 443 alignment errors^{53,54}. From the three independent reconstructions, transformation matrices were computed to align

444 the three tilt series to a global coordinate system. The three aligned tilt series were collectively reconstructed by
 445 RESIRE using the same angular and spatial refinement procedure, which produced the final scalar tomography
 446 reconstruction. The transformation matrices obtained from the scalar tomography were used for the vector
 447 tomography reconstruction.

448 **The vector tomography reconstruction.** The 3D magnetization vector field was reconstructed by taking the
 449 difference of the left- and right-circularly polarized projections of the six experimental tilt series, producing three
 450 independent tilt series with the magnetic contrast. The vector tomography algorithm is modelled as a least squares
 451 optimization problem and solved directly by gradient descent. The least squares problem is given as,

$$\begin{aligned} \min_{O_1, O_2, O_3} f(O_1, O_2, O_3) &= \sum_{i=1}^N \|\alpha_i \Pi_i O_1 + \beta_i \Pi_i O_2 + \gamma_i \Pi_i O_3 - b_i\|^2 \\ &= \sum_{i=1}^N \|\Pi_i(\alpha_i O_1 + \beta_i O_2 + \gamma_i O_3) - b_i\|^2 \quad , \quad (4) \end{aligned}$$

452 where O_1, O_2, O_3 are the three components of the vector field to be reconstructed, N is the number of the
 453 projections of the three tilt series, Π_i is the projection operator with respect to the Euler angle set $\{\phi_i, \theta_i, \psi_i\}$, and b_i
 454 is the experimentally measured projection. $\{\alpha_i, \beta_i, \gamma_i\}$ are the coefficient set with respect to the projection operator
 455 and are related to the corresponding Euler angle set by,

$$\alpha_i = \sin \theta_i \cos \phi_i, \quad \beta_i = \sin \theta_i \sin \phi_i, \quad \alpha_i = \cos \theta_i \quad . \quad (5)$$

456 The least square problem is solved via gradient descent and the gradients are computed by,

$$\begin{aligned} \nabla_{O_1} f(O_1, O_2, O_3) &= \sum_{i=1}^N \alpha_i \Pi_i^T \Pi_i(\alpha_i O_1 + \beta_i O_2 + \gamma_i O_3) \\ \nabla_{O_2} f(O_1, O_2, O_3) &= \sum_{i=1}^N \beta_i \Pi_i^T \Pi_i(\alpha_i O_1 + \beta_i O_2 + \gamma_i O_3) \quad . \quad (6) \\ \nabla_{O_3} f(O_1, O_2, O_3) &= \sum_{i=1}^N \gamma_i \Pi_i^T \Pi_i(\alpha_i O_1 + \beta_i O_2 + \gamma_i O_3) \end{aligned}$$

457 The $(j+1)^{\text{th}}$ iteration of the algorithm is updated as,

$$\begin{aligned} O_1^{j+1} &= O_1^j - t \nabla_{O_1} f(O_1, O_2, O_3) = O_1^j - t \sum_{i=1}^N \alpha_i \Pi_i^T \Pi_i(\alpha_i O_1^j + \beta_i O_2^j + \gamma_i O_3^j) \\ O_2^{j+1} &= O_2^j - t \nabla_{O_2} f(O_1, O_2, O_3) = O_2^j - t \sum_{i=1}^N \beta_i \Pi_i^T \Pi_i(\alpha_i O_1^j + \beta_i O_2^j + \gamma_i O_3^j) \quad , \quad (7) \\ O_3^{j+1} &= O_3^j - t \nabla_{O_3} f(O_1, O_2, O_3) = O_3^j - t \sum_{i=1}^N \gamma_i \Pi_i^T \Pi_i(\alpha_i O_1^j + \beta_i O_2^j + \gamma_i O_3^j) \end{aligned}$$

458 where t is the step size. For a given tilt angle set $\{\phi_i, \theta_i, \psi_i\}$, the forward projection of a 3D object is computed
 459 using the Fourier slice theorem, while the back projection is implemented by linear interpolation.

460 To validate the vector tomography reconstruction algorithm, we used a structural model consisting of
 461 TMMs/anti-TMMs and calculated their diffraction patterns based on the experimental parameters. After adding
 462 noise to the diffraction patterns, we performed ptychographic reconstructions to generate projections. Using the
 463 vector tomography reconstruction algorithm, we were able to reconstruct the 3D magnetization vector field of the
 464 majority TMMs/anti-TMMs from the projections. After validating the vector tomography algorithm using model

465 data, we applied it to reconstruct the 3D magnetization vector field of the ferromagnetic meta-lattice from the
 466 experimentally measured tilt series.

467 **Quantification of the 3D spatial resolution.** We quantified the spatial resolution using two independent methods.
 468 First, we divided the 91 projections of three tilt series into two halves by choosing alternate projections and
 469 conducted two independent 3D scalar reconstructions, from which two different supports were generated to
 470 separate the nickel from the silica region. We then performed two independent vector reconstructions from the
 471 two halves. After applying the support to exclude the silica region, we calculated the Fourier shell correlation
 472 (FSC) from the two 3D vector reconstructions. Extended Data Fig. 7a-f shows the FSC for $|m_x|$, $|m_y|$, $|m_z|$,
 473 $|m_{xy}|$, $|m_{xz}|$ and $|m_{yz}|$, respectively, where m_x , m_y , and m_z are the x -, y -, and z -component of the unnormalized
 474 magnetization vector field and $|m_{xy}| = \sqrt{m_x^2 + m_y^2}$, $|m_{xz}| = \sqrt{m_x^2 + m_z^2}$ and $|m_{yz}| = \sqrt{m_y^2 + m_z^2}$. As m_x , m_y ,
 475 and m_z have both positive and negative values (Supplementary Video 1), their Fourier coefficients in some
 476 resolution shells have small values. To avoid dividing by small values, we computed the FSC for the magnitude
 477 of m_x , m_y and m_z . According to the cut-off of FSC = 0.143, a criterion commonly used in cryo-electron
 478 microscopy⁵⁵, we characterized the 3D spatial resolution of the vector reconstruction to be 10 nm. We noted that
 479 the FSC values for $|m_z|$ are slightly smaller than 0.143 at some high spatial frequency (Extended Data Fig. 7c).
 480 This was because only a half of the projections were used to perform each 3D vector reconstruction. Compared
 481 to cryo-electron microscopy that employs a large number of images for a 3D reconstruction⁵⁵, the number of
 482 projections in our experiment is much smaller. Thus, when only a half of the projections were used for the vector
 483 reconstruction, the spatial resolution was reduced especially along the beam (z) direction. Second, we quantified
 484 three TMM and anti-TMM pairs distributed along the x -, y - and z -axis in the 3D vector reconstruction (Extended
 485 Data Fig. 7g-o). The net topological charge of each TMM and anti-TMM pair was calculated to be $Q = 0$, while
 486 the topological charge of the TMM and anti-TMM in each pair was computed to be $Q = +1$ (red dot) and -1 (green
 487 dot), respectively. The distance between the red and green dot in each pair is 2 voxels with a voxel size of 5 nm,
 488 further demonstrating that a spatial resolution of 10 nm was achieved along the x -, y - and z -axis.

489 **Calculation of the TMM density and charge.** We first calculated the topological charge density of every voxel
 490 ($5 \times 5 \times 5 \text{ nm}^3$) within the volume of the meta-lattice by discretizing the expression $\rho = \frac{3}{4\pi} \partial_x \mathbf{n} \cdot (\partial_y \mathbf{n} \times \partial_z \mathbf{n})$ on a
 491 cubic lattice, producing a 3D map of the local maxima (positive) and minima (negative) of the charge density. At
 492 each local extremum, we chose $3 \times 3 \times 3$ vectors surrounding the local extremum. To compute the topological
 493 charge enclosed by these vectors, we triangulated the surface and calculated the solid angle (ω) of each triangle
 494 surface subtended by three vectors ($\mathbf{n}_1, \mathbf{n}_2, \mathbf{n}_3$),

$$495 \quad \tan \frac{\omega}{2} = \frac{\mathbf{n}_1 \cdot (\mathbf{n}_2 \times \mathbf{n}_3)}{1 + \mathbf{n}_1 \cdot \mathbf{n}_2 + \mathbf{n}_1 \cdot \mathbf{n}_3 + \mathbf{n}_2 \cdot \mathbf{n}_3} \quad . \quad (8)$$

496 The topological charge was evaluated by $Q = \frac{1}{4\pi} \sum_{\text{facets}} \omega$, which is an integer as the summation of all solid angles
 497 over an enclosed surface is an integer number of 4π . We evaluated the topological charge of the magnetic voids
 498 using the same approach.

499 **Atomistic simulations using the experimental data as direct input.** Four $15 \times 15 \times 15 \text{ nm}^3$ volumes of the
 500 experimentally determined 3D magnetization vector field were extracted from the ferromagnetic meta-lattice as
 501 direct input to atomistic simulations. The four volumes contain two TMMs and two anti-TMMs, each of which is

502 located close to the centre of each volume. A nickel fcc lattice with a lattice constant of 3.524 Å was constructed
 503 for each volume and all atomic sites within each 5×5×5 nm³ voxel were mapped to the same normalized
 504 magnetization vector determined from the experiment, yielding a total of 296,352 atomistic spins in each volume.
 505 The dynamics of the individual atomistic spins is described by the Landau-Lifshitz-Gilbert equation of motion⁵⁶,

$$506 \quad \frac{\partial \mathbf{S}_i}{\partial t} = -\frac{\gamma}{\mu_m(1+\lambda^2)} [\mathbf{S}_i \times \mathbf{H}_{\text{eff}}^i + \lambda \mathbf{S}_i \times (\mathbf{S}_i \times \mathbf{H}_{\text{eff}}^i)] \quad , \quad (9)$$

507 where \mathbf{S}_i is a unit vector at atomistic site i , γ is the gyromagnetic ratio, λ is the phenomenological coupling
 508 constant (damping) and μ_m is the magnetic moment. $\mathbf{H}_{\text{eff}}^i$, given by equation (11), is the effective magnetic field
 509 at site i . The total energy of the system is represented by the following atomistic spin Hamiltonian,

$$510 \quad \mathcal{H} = -J \sum_{\langle ij \rangle} \mathbf{S}_i \cdot \mathbf{S}_j - k_u \sum_i (S_i^z)^2 - \mu_m \mathbf{B} \cdot \sum_i \mathbf{S}_i \quad , \quad (10)$$

511 where the first term on the right hand side is the exchange interaction between spins at site i and j , the second is
 512 the uniaxial anisotropy term, and the third is the Zeeman term. The exchange constant (J) and the magnetic
 513 moment (μ_m) are 2.757×10^{-21} Joules per link and 0.606 Bohr magnetons, respectively⁵⁷. The anisotropy constant,
 514 k_u , and the external field \mathbf{B} were neglected in the simulations. The above Hamiltonian can be represented as an
 515 effective magnetic field for the spin at site i by taking the negative first derivative,

$$516 \quad \mathbf{H}_{\text{eff}}^i = -\frac{\partial \mathcal{H}}{\partial \mathbf{S}_i} \quad . \quad (11)$$

517 Based on these equations, we performed atomistic simulations of each volume by fixing the spins on the outer
 518 boundary of the volume. All the other spins were allowed to relax to an equilibrium configuration. After 50 ps, a
 519 stable TMM or anti-TMM formed in each volume with a topological charge matching the experimental value
 520 (Extended Data Fig. 10a-d). Further simulations showed that if the atomistic spins on the outer boundary were
 521 fixed, any random spin configuration within each volume yielded identical results. We also conducted atomistic
 522 simulations to determine how much of the boundary can be relaxed before each TMM becomes unstable. We
 523 found that as long as the atomistic spins were fixed on four of the six surfaces of each volume, the TMM remained
 524 stable inside the volume (Extended Data Fig. 10e-h). All these atomistic simulation results confirm that surface
 525 constraints can stabilize TMMs.

526 **Data availability**

527 All the experimental data are available at <https://doi.org/10.5281/zenodo.5450910>.

528 **Code availability**

529 The MATLAB source codes for the scalar and vector tomography reconstruction algorithms and data analysis
 530 used in this work are available at <https://doi.org/10.5281/zenodo.5450910>.

- 531 39. Watanabe, R. *et al.* Extension of size of monodisperse silica nanospheres and their well-ordered
 532 assembly. *J. Colloid Interface Sci.* **360**, 1-7 (2011).
 533 40. Russell, J. L., Noel, G. H., Warren, J. M., Tran, N.-L. L. & Mallouk, T. E. Binary colloidal crystal
 534 films grown by vertical evaporation of silica nanoparticle suspensions. *Langmuir* **33**, 10366-10373
 535 (2017).
 536 41. Mahale, P. *et al.* Oxide-Free Three-Dimensional Germanium/Silicon Core-Shell Metalattice Made by
 537 High-Pressure Confined Chemical Vapor Deposition. *ACS Nano* **14**, 12810-12818 (2020).

- 538 42. Regan, T. J. *et al.* Chemical effects at metal/oxide interfaces studied by x-ray-absorption spectroscopy.
539 *Phys. Rev. B* **64**, 214422 (2001).
- 540 43. Lambers, E. C. *et al.* Room-temperature oxidation of Ni(110) at low and atmospheric oxygen
541 pressures. *Oxid. Met.* **45**, 301-321 (1996).
- 542 44. Shapiro, D. A. *et al.* An ultrahigh-resolution soft x-ray microscope for quantitative analysis of
543 chemically heterogeneous nanomaterials. *Sci. Adv.* **6**, eabc4904 (2020).
- 544 45. Eisebitt, S. *et al.* Lensless imaging of magnetic nanostructures by X-ray spectro-holography. *Nature*
545 **432**, 885–888 (2004).
- 546 46. Marchesini, S. *et al.* SHARP: a distributed GPU-based ptychographic solver. *J. Appl. Crystallogr.* **49**,
547 1245-1252 (2016).
- 548 47. Goldstein, R. M., Zebker, H. A. & Werner, C. L. Satellite radar interferometry: Two-dimensional phase
549 unwrapping. *Radio Sci.* **23**, 713–720 (1988).
- 550 48. McNaught, A.D. and Wilkinson, A. *Compendium of Chemical Terminology* 2nd edn (Int. Union Pure
551 Appl. Chem., 1997).
- 552 49. Yang, Y. *et al.* Determining the three-dimensional atomic structure of an amorphous solid. *Nature* **592**,
553 60-64 (2021).
- 554 50. Hannon, J. P., Trammell, G. T., Blume, M. & Gibbs, D. X-ray resonance exchange scattering. *Phys.*
555 *Rev. Lett.* **61**, 1245 (1988).
- 556 51. Scott, M. C. *et al.* Electron tomography at 2.4-ångström resolution. *Nature* **483**, 444-447 (2012).
- 557 52. Chen, C.-C. *et al.* Three-dimensional imaging of dislocations in a nanoparticle at atomic resolution.
558 *Nature* **496**, 74-77 (2013).
- 559 53. Pham, M., Yuan, Y., Rana, A., Miao, J. & Osher, S. RESIRE: real space iterative reconstruction engine
560 for Tomography. *arXiv:2004.10445* (2020).
- 561 54. Yuan, Y. *et al.* Three-dimensional atomic packing in amorphous solids with liquid-like structure. *Nat.*
562 *Mater.* **21**, 95–102 (2022).
- 563 55. Scheres, S. H. W. & Chen, S. Prevention of overfitting in cryo-EM structure determination. *Nat.*
564 *Methods* **9**, 853-854 (2012).
- 565 56. Gilbert, T. L. A phenomenological theory of damping in ferromagnetic materials. *IEEE Trans. Magn.*
566 **40**, 3443-3449 (2004).
- 567 57. Evans, R. F. L. *et al.* Atomistic spin model simulations of magnetic nanomaterials. *J. Phys.: Condens.*
568 *Matter* **26**, 103202 (2014).
- 569

1

1. Extended Data

2

Figure or Table # Please group Extended Data items by type, in sequential order. Total number of items (Figs. + Tables) must not exceed 10.	Figure/Table title One sentence only	Filename Whole original file name including extension. i.e.: Smith_ED_Fig1.jpg	Figure/Table Legend If you are citing a reference for the first time in these legends, please include all new references in the main text Methods References section, and carry on the numbering from the main References section of the paper. If your paper does not have a Methods section, include all new references at the end of the main Reference list.
Extended Data Fig. 1	Magnetic hysteresis measurements of a Ni meta-lattice and a Ni thin film	Miao_ED_Fig1.jpg	5 T field sweep measurements of the hysteresis loops of the Ni meta-lattice and Ni thin film at 3 K and 305 K, where the inset shows the magnified hysteresis loops at 305 K. The experiments were performed with a Quantum Design MPMS SQUID magnetometer, and a diamagnetic background subtraction was implemented by subtracting off the average of two linear fits to the data at high positive and negative fields, beyond the saturation of the samples. The thickness of the meta-lattice varies from 400 to 450 nm, measured by a scanning electron microscope. As the meta-lattice has an fcc structure (Extended Data Fig. 6), the effective thickness of Ni in the meta-lattice was estimated to be 110.5 nm by considering the fcc packing efficiency of 74%. As a comparison, a pure Ni thin film of 200 nm thick was characterized by the same experimental procedure. The hysteresis loops of the Ni meta-lattice and the Ni thin film show similar remanent magnetization and saturation magnetization at both 3 K and 305 K. The slight differences of the remanent magnetization and saturation magnetization between the Ni meta-lattice and the Ni thin film are due to two factors: i) the thickness of the meta-lattice varies from 400 to 450 nm; and ii) the experimental packing efficiency of the sample may deviate from the theoretical value of 74%.

Extended Data Fig. 2	Sample preparation	Miao_ED_Fig2.jpg	<p>a, b, Optical microscopy images of the meta-lattice sample, prepared by FIB milling. The sample was mounted on a 3-mm transmission electron microscopy grid and glued on a copper ring (b). c-f, Scanning electron microscopy images of the sample. The mounting geometry of the sample is important for the soft x-ray vector ptychotomography experiment with three in-place rotation angles. The meta-lattice sample was thinned to 150 nm by a FIB (f), allowing the sample to be tilted to high angles. g, X-ray absorption spectroscopy of the Ni meta-lattice sample (red curve). For a comparison, the x-ray absorption spectra of a pure Ni film (blue curve) and a NiO film (green curve) are adapted from ref. 41. The three grey arrows indicate that the L_3 peak position of the meta-lattice agrees well with that of pure Ni, while the NiO L_3 peak is shifted to a higher energy. The black arrow shows that the absorption coefficients of the meta-lattice are in good agreement with those of pure Ni in the energy range from 885 eV to 870 eVs, but NiO has smaller values due to sp-hybridization. The purple arrow indicates that the L_2 peak of the meta-lattice is more consistent with that of pure Ni than of NiO.</p>
Extended Data Fig. 3	Improvement of the ptychography reconstruction	Miao_ED_Fig3.jpg	<p>a, The ptychography reconstruction of a representative projection with a small number of corrupted diffraction patterns, where reconstruction artifacts are clearly visible. The corrupted diffraction patterns were resulted from detector readout malfunction or unstable x-ray flux. b, The same reconstructed projection after the removal of the corrupted diffraction patterns. c, The ptychography reconstruction of a representative high tilt projection, in which artefacts were induced by phase unwrapping. d, The same reconstructed projection after phase unwrapping was enforced in the reconstruction. Scale bar, 200 nm.</p>
Extended Data Fig. 4	3D structural characterization of	Miao_ED_Fig4.jpg	<p>a-c, The experimentally reconstructed 3D electron density of the meta-lattice is oriented along the [100], [110] and</p>

	the ferromagnetic meta-lattice		[111] directions with red, yellow and blue representing high, medium and low density, respectively. d-f , The corresponding 2D power spectrum of the projections along the [100], [110] and [111] directions, in which the Bragg peaks are clearly visible. Scale bar, 200 nm.
Extended Data Fig. 5	Structural characterization of the sample with scanning transmission electron microscopy (STEM).	Miao_ED_Fig5.jpg	a , An annual dark-field STEM image of the meta-lattice, where the rectangle with dashed lines represents the reconstruction region by soft x-ray vector ptychotomography and the square with solid lines shows a more ordered region. The circle indicates some imperfections in the sample. Scale bar, 200 nm. b , 2D power spectrum of the STEM image, where the sharp Bragg peaks indicate that the meta-lattice is ordered. c , Histograms of the nearest-neighbour distances between the TMM and anti-TMM, TMM and TMM, anti-TMM and anti-TMM pairs in the more ordered region (square with solid lines in a), which is consistent with Fig. 3d-f, obtained from the region with some imperfections (rectangle with dashed lines in a).
Extended Data Fig. 6	Difference of a left- and a right-circularly polarized projection of the ferromagnetic meta-lattice.	Miao_ED_Fig6.jpg	a, b , Representative left- and right-circularly polarized projections, respectively. c , The difference of the left- and right-circularly polarized projections, showing the comparable charge and magnetic contrast of the meta-lattice in our experiment. The colour bars are in arbitrary units and the values of the color bars are consistent in (a-c) . Scale bar, 100 nm.
Extended Data Fig. 7	Quantification of the 3D spatial resolution of the vector reconstruction.	Miao_ED_Fig7.jpg	a-f , FSC for $ m_x $, $ m_y $, $ m_z $, $ m_{xy} $, $ m_{xz} $ and $ m_{yz} $, respectively, where m_x , m_y , and m_z are the x-, y-, and z-component of the unnormalized magnetization vector field with $ m_{xy} = \sqrt{m_x^2 + m_y^2}$, $ m_{xz} = \sqrt{m_x^2 + m_z^2}$ and $ m_{yz} = \sqrt{m_y^2 + m_z^2}$. The FSC curves were calculated from two independent vector reconstructions of the meta-lattice. According to the criterion of FSC = 0.143 (dashed lines), a

			<p>3D spatial resolution of 10 nm was achieved with soft x-ray vector ptycho-tomography, which corresponds to a spatial frequency of 0.1 nm^{-1}. The FSC values for m_z are slightly smaller than 0.143 at some high spatial frequency because only a half of the projections were used to perform each 3D vector reconstruction (Methods). Three TMM and anti-TMM pairs distributed along the x- (g-i), y- (j-l) and z-axis (m-o) in the 3D vector reconstruction. The net topological charge of each pair was calculated to be $Q = 0$, while the topological charge of the TMM and anti-TMM in each pair was computed to be $Q = +1$ (red dot) and -1 (green dot), respectively. The distance between the red and green dot in each pair is 2 voxels with a voxel size of 5 nm, demonstrating that a spatial resolution of 10 nm was achieved along the x-, y- and z-axis.</p>
Extended Data Fig. 8	The emergent magnetic field of real and virtual TMMs.	Miao_ED_Fig8.jpg	<p>a, b, The emergent magnetic field of the TMM and anti-TMM shown in Fig. 2c and e in the main text, respectively. The vector plots indicate that the TMM and anti-TMM form a source and a sink of the emergent magnetic field, respectively. c, d, The emergent magnetic field of the virtual TMM and anti-TMM shown in Fig. 4a and b, respectively. The red and blue cones represent outflow and inflow of the emergent magnetic field, respectively, while the cone size indicates the total emergent flux through the facet. Note that while there is both outflow and inflow of the emergent magnetic field in each case, the net flow corresponds to a source and sink, respectively. The scale bars, 5 nm (a) and 15 nm (c).</p>
Extended Data Fig. 9	Effects of the experimental errors and statistical fluctuations on the analysis of TMMs.	Miao_ED_Fig9.jpg	<p>a-c, Histograms of the topological charges calculated from equation (1) after adding random angular fluctuations to the experimentally measured magnetization vectors with a standard deviation of 2° (a), 15° (b) and 20° (c). d-l, Histograms of the nearest-neighbour distances of the TMM and anti-TMM, TMM and TMM, anti-TMM and anti-TMM pairs for the angular fluctuation of 2° (d-f), 15° (g-i) and</p>

			20° (j-l), which are consistent with those without the introduction of the angular fluctuation (Fig. 3d-f).
Extended Data Fig. 10	Atomistic simulations using the experimental data as direct input.	Miao_ED_Fig10.jpg	Four 15×15×15 nm ³ volumes were extracted from the ferromagnetic meta-lattice, containing two TMMs and two anti-TMMs. The atomistic spins were fixed on the outer boundary of each volume, while all the other spins were allowed to relax to an equilibrium configuration. After 50 ps, a stable TMM or anti-TMM formed in each volume with a topological charge matching the experimental value. a-d , Two stable TMMs (red dots) and two anti-TMMs (blue dots) after relaxation, respectively, which are consistent with the experimental results. With the atomistic spins fixed on four of the six surfaces of each volume, the two TMMs and two anti-TMMs remained stable inside the volumes (e-h). Scale bar, 5 Å.

3

4

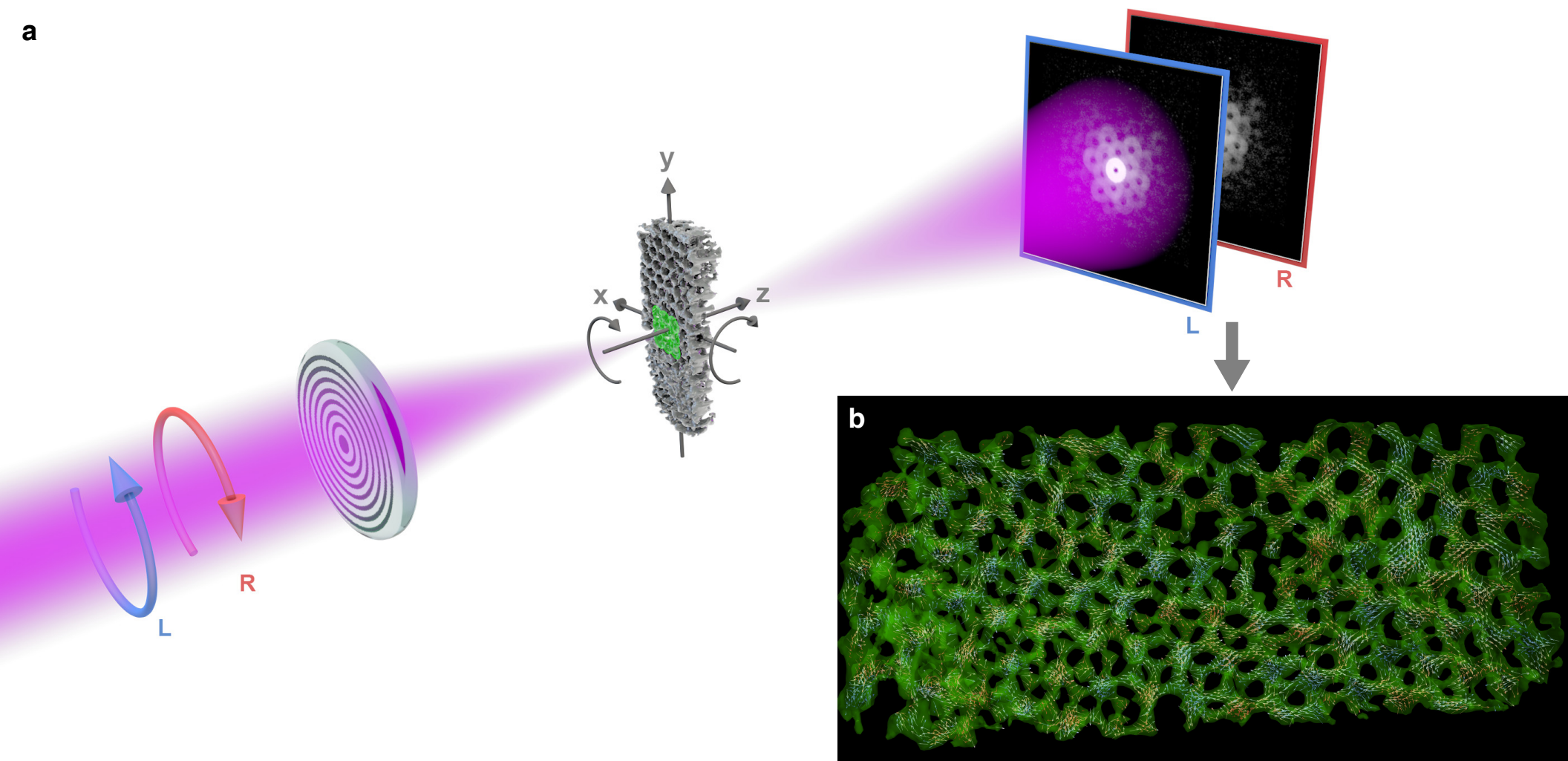
2. Supplementary Information:

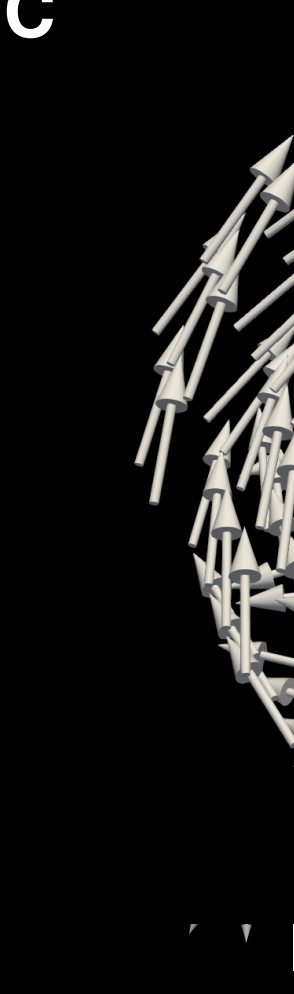
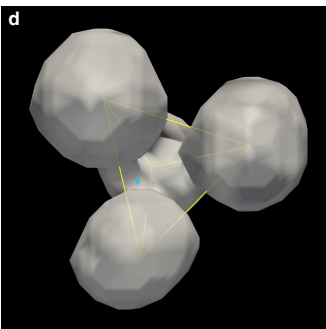
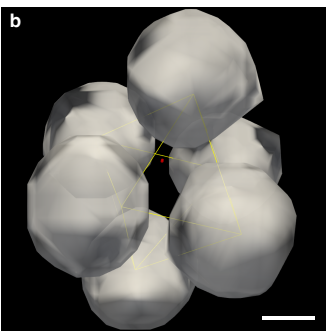
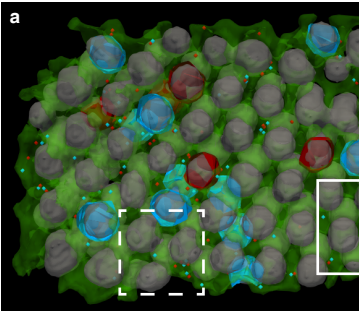
5

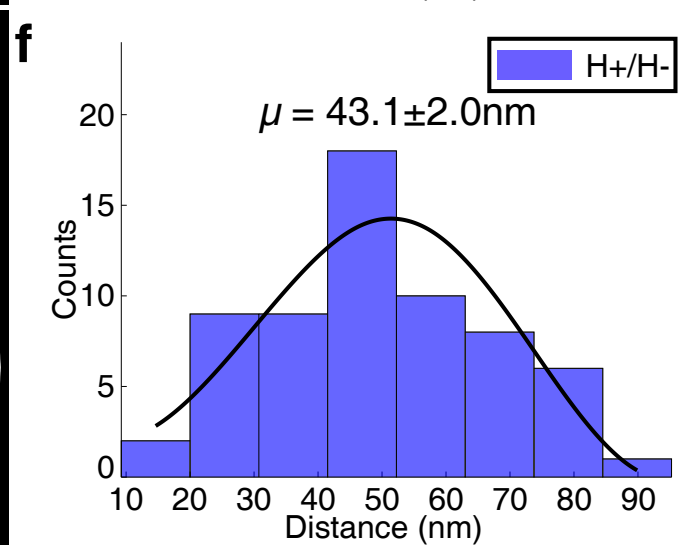
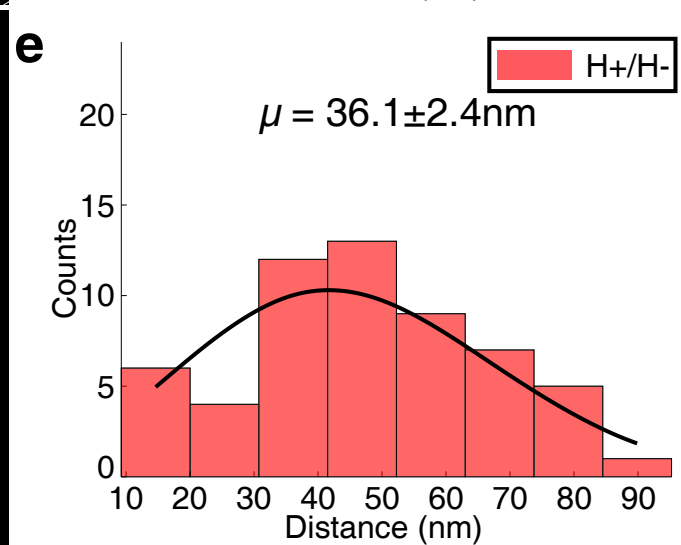
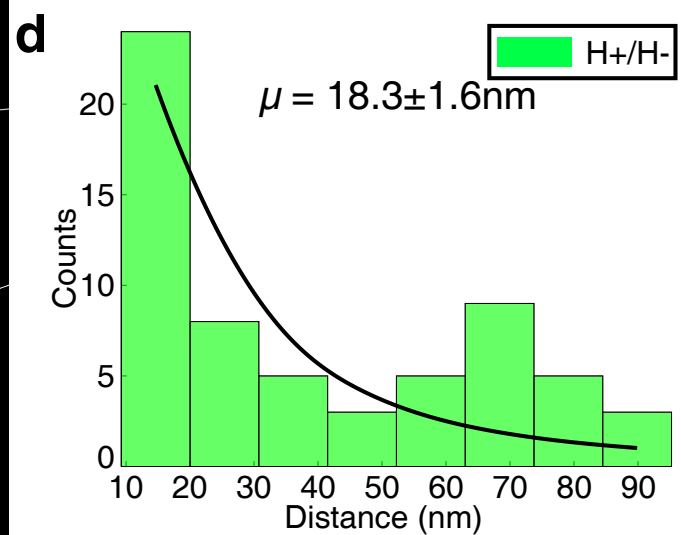
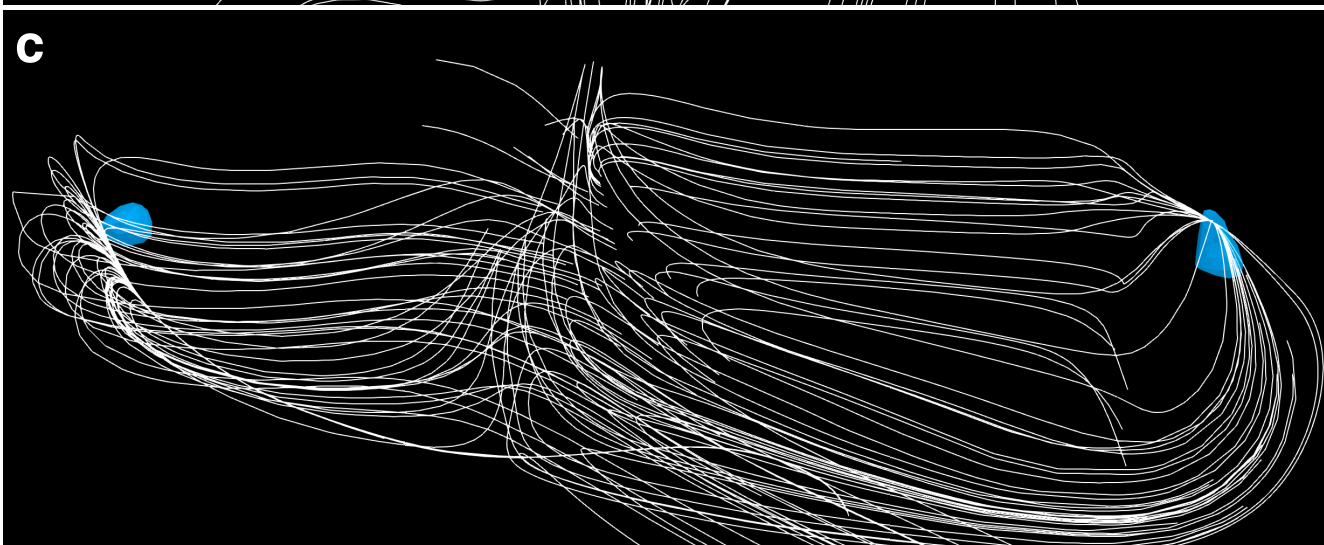
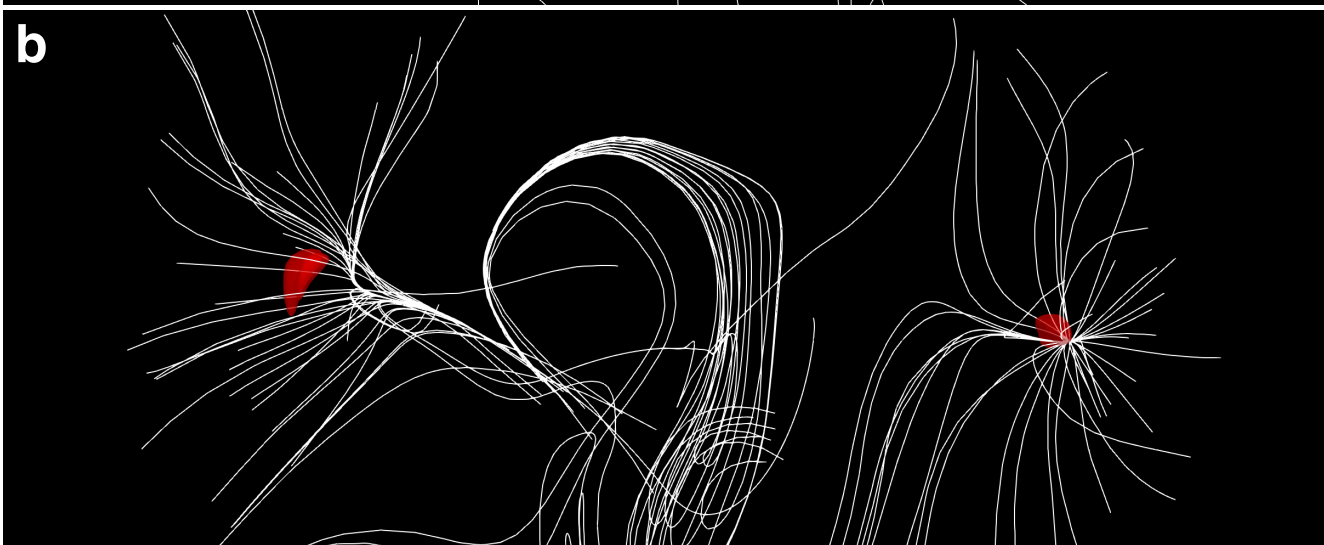
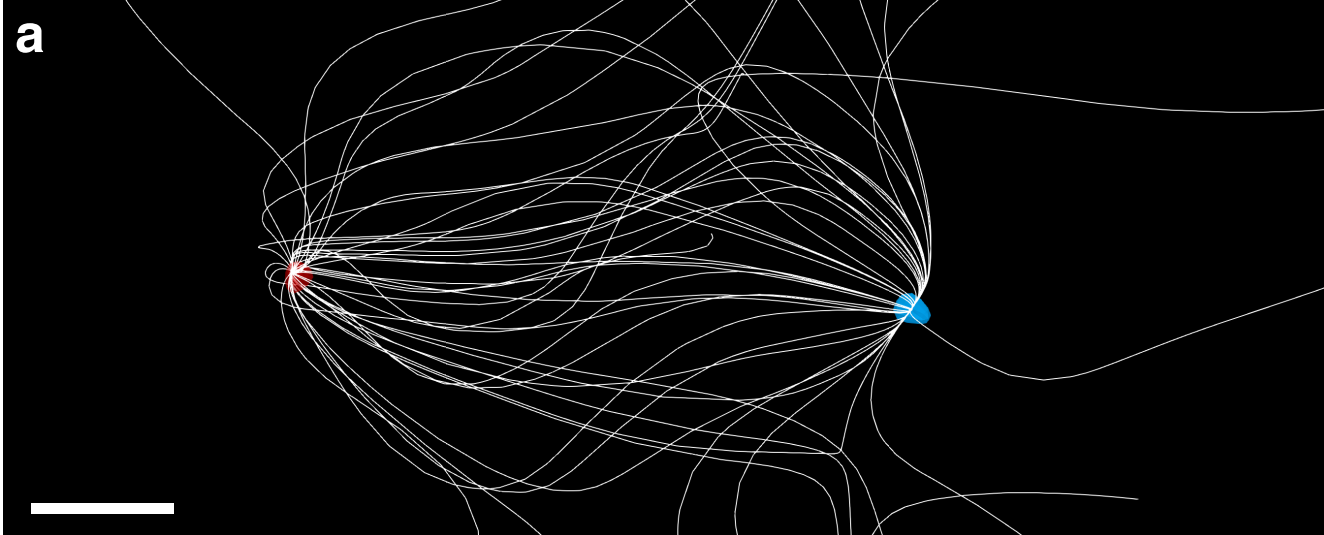
6

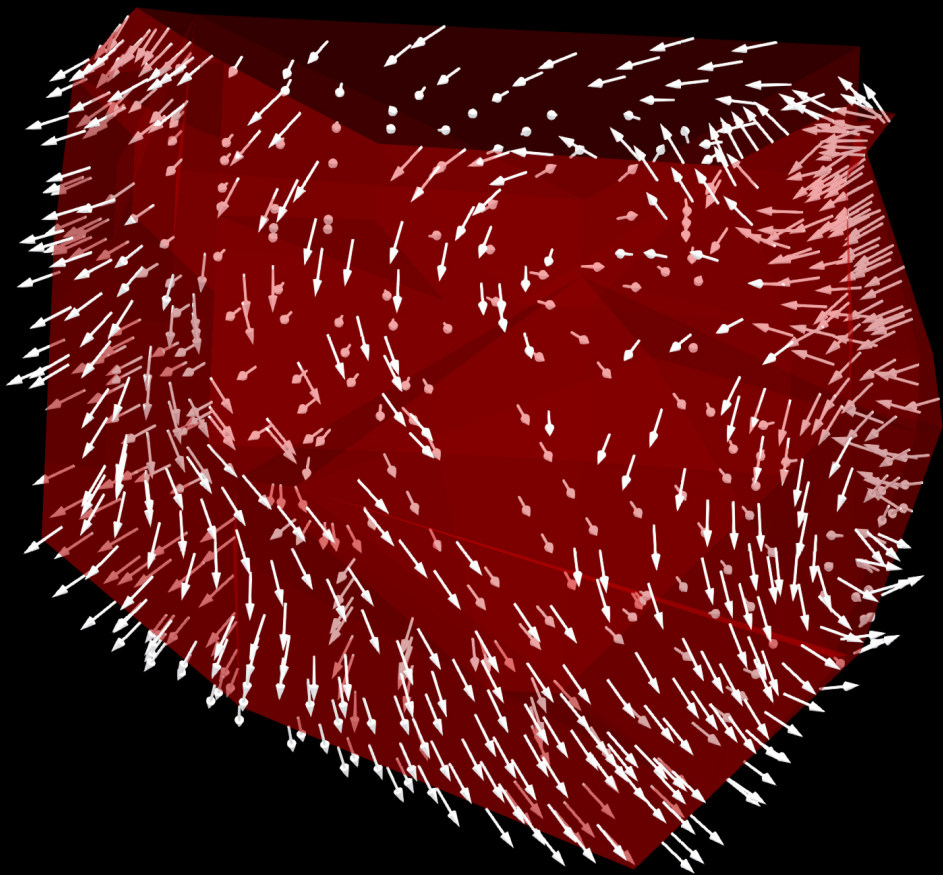
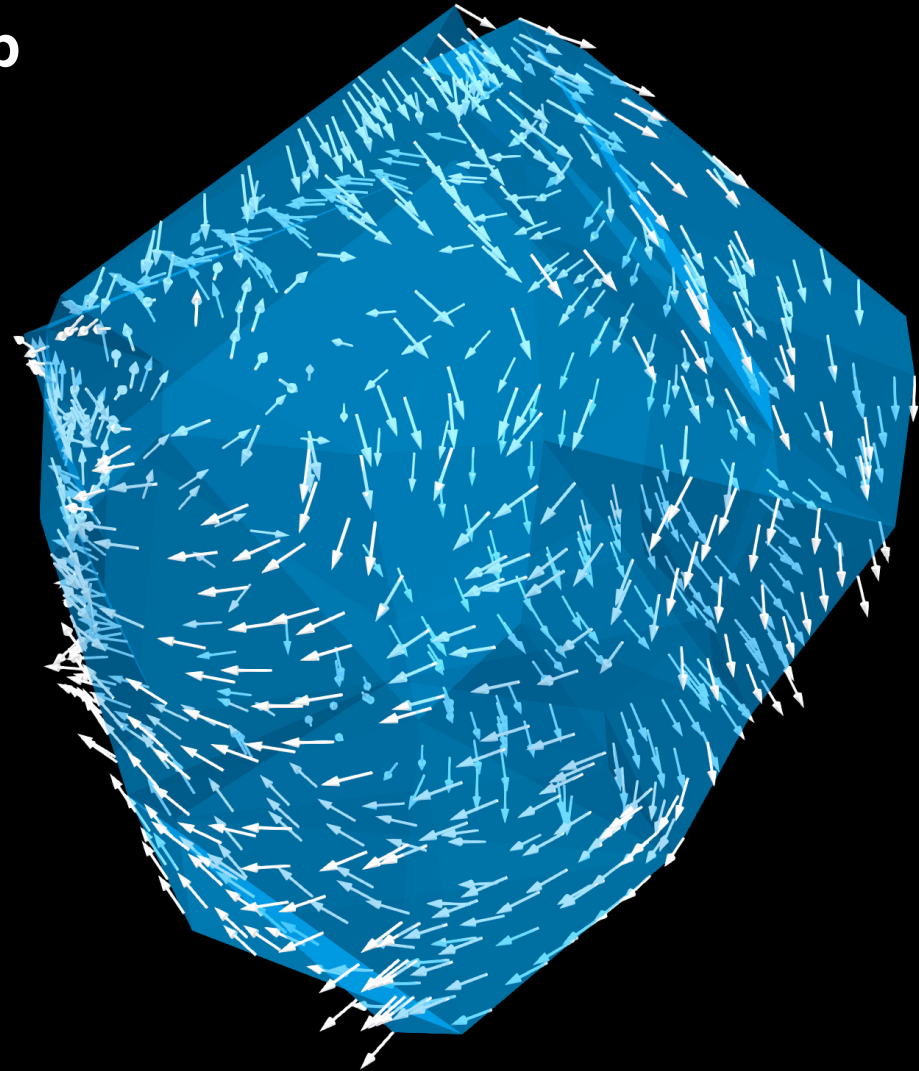
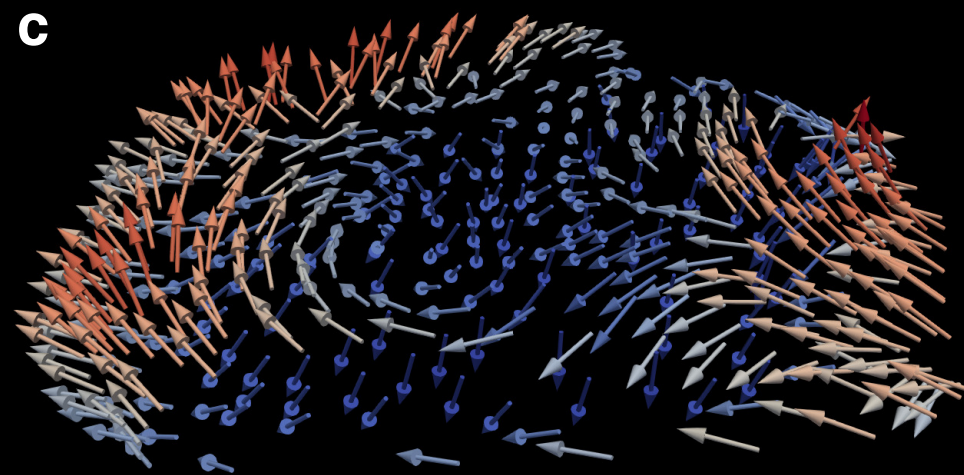
Type	Number Each type of file (Table, Video, etc.) should be numbered from 1 onwards. Multiple files of the same type should be listed in sequence, i.e.: Supplementary Video 1, Supplementary Video 2, etc.	Filename Whole original file name including extension. i.e.: <i>Smith_Supplementary_Video_1.mov</i>	Legend or Descriptive Caption Describe the contents of the file
Supplementary Video	Supplementary Video 1	Miao_Supplementary_Video_1.mp4	3D scalar (green) and vector (arrow) reconstructions of the ferromagnetic meta-lattice. The global view of the 3D magnetization vector field zooms in to show a TMM and

			<p>anti-TMM pair (Fig. 3a), a TMM and TMM pair (Fig. 3b), an anti-TMM and anti-TMM pair (Fig. 3c), where TMMs and anti-TMMs are indicated by red and blue dots, respectively. In each magnified view, the global field fades away and the local magnetization vector field around each topological monopole is given by gray arrows. The field lines follow the emergent magnetic field.</p>
Supplementary Video	Supplementary Video 2	Miao_Supplementary_Video_2.mp4	<p>3D spatial distribution of 68 TMMs (red dots) and 70 anti-TMMs (blue dots) in the ferromagnetic meta-lattice, where 8 virtual TMMs and 11 virtual anti-TMMs are labelled with red and blue blobs (triangulated surfaces), respectively. The silica nanospheres are rendered as gray iso-surfaces.</p>

a**b**





a**b****c****d**